



# The Importance of Star Formation Intensity in Ly $\alpha$ Escape from Green Pea Galaxies and Lyman Break Galaxy Analogs

Keunho Kim<sup>1</sup> , Sangeeta Malhotra<sup>1,2</sup> , James E. Rhoads<sup>1,2</sup> , Nathaniel R. Butler<sup>1</sup> , and Huan Yang<sup>3</sup>

<sup>1</sup>School of Earth & Space Exploration, Arizona State University, Tempe, AZ 85287, USA; [Keunho.Kim@asu.edu](mailto:Keunho.Kim@asu.edu)

<sup>2</sup>NASA Goddard Space Flight Center, Greenbelt, MD 20770, USA

<sup>3</sup>Las Campanas Observatory, Carnegie Institution for Science, Chile

Received 2019 September 9; revised 2020 February 19; accepted 2020 February 19; published 2020 April 23

## Abstract

We have studied ultraviolet images of 40 Green Pea galaxies and 15 local Lyman Break Galaxy Analogs to understand the relation between Ly $\alpha$  photon escape and central UV photometric properties. We measured star-formation intensity (SFI; star formation rate per unit area) from the central 250 pc region ( $S_{250\text{ pc}}$ ) using Cosmic Origins Spectrograph near-ultraviolet images from the *Hubble Space Telescope*. The measured  $S_{250\text{ pc}}$  of our sample Green Peas ranges from  $2.3\text{--}46 M_{\odot} \text{ yr}^{-1} \text{ kpc}^{-2}$ , with a geometric mean of  $15 M_{\odot} \text{ yr}^{-1} \text{ kpc}^{-2}$  and a standard deviation of 0.266 dex, forming a relatively narrow distribution. The Lyman Break Galaxy Analogs show a similarly narrow distribution of  $S_{250\text{ pc}}$  (0.271 dex), though with a larger mean of  $28 M_{\odot} \text{ yr}^{-1} \text{ kpc}^{-2}$ . We show that while the Ly $\alpha$  equivalent width ( $\text{EW}(\text{Ly}\alpha)$ ) and the Ly $\alpha$  escape fraction ( $f_{\text{esc}}^{\text{Ly}\alpha}$ ) are not significantly correlated with the central SFI ( $S_{250\text{ pc}}$ ), both are positively correlated with the ratio of surface brightness to galaxy stellar mass ( $S_{250\text{ pc}}/M_{\text{star}}$ ), with correlation coefficients ( $p$ -values) of 0.702 ( $1 \times 10^{-8}$ ) and 0.529 ( $5 \times 10^{-4}$ ) with  $\text{EW}(\text{Ly}\alpha)$  and  $f_{\text{esc}}^{\text{Ly}\alpha}$ , respectively. These correlations suggest a scenario where intense central star formation can drive a galactic wind in galaxies with relatively shallow gravitational potential wells, thus clearing channels for the escape of Ly $\alpha$  photons.

*Unified Astronomy Thesaurus concepts:* Compact galaxies (285); Starburst galaxies (1570); Galaxy formation (595); Galaxy evolution (594); Galaxy structure (622); Star formation (1569); Reionization (1383)

## 1. Introduction

Green Pea (GP) galaxies are a class of local starburst galaxies that were discovered by the citizen science “Galaxy Zoo” project based on the Sloan Digital Sky Survey (SDSS; Lintott et al. 2008). As inferred from their nickname, their optical color is greenish due to their strong [O III]  $\lambda 5007$  emission line at their redshifts (i.e.,  $0.1 \lesssim z \lesssim 0.35$ ), and their morphology seen in SDSS images is mostly compact and unresolved (e.g., Cardamone et al. 2009). Studies on GPs have shown that they are low stellar mass ( $8 \lesssim \log(M_{\text{star}}/M_{\odot}) \lesssim 10$ ) and metal-poor galaxies for their stellar mass with typically low intrinsic extinction ( $E(B - V) \lesssim 0.2$ ) and high [O III]/[O II] ratios, experiencing intense star formation activities (i.e.,  $10^{-7} \text{ yr}^{-1} \lesssim \text{sSFR}$ ) (e.g., Amorín et al. 2010; Izotov et al. 2011; Jaskot & Oey 2013; Yang et al. 2016, 2017, and references therein). In particular, their UV properties have shown that the majority of GPs are Ly $\alpha$ -emitters (LAEs) and some of which have been confirmed as Lyman-continuum (LyC) leakers (e.g., Henry et al. 2015; Izotov et al. 2016, 2018b; Yang et al. 2016, 2017; Orlitová et al. 2018).

In the field of cosmology, LyC leakers are important possible contributors for reionizing the early universe ( $z > 6$ ). Therefore, in consideration of the associations between LAEs and LyC leakers (e.g., Verhamme et al. 2015; de Barros et al. 2016; Izotov et al. 2016), searching for LAEs and understanding the Ly $\alpha$  escape mechanisms is of astrophysical interest (e.g., Ahn et al. 2003; Verhamme et al. 2006; Gronke & Dijkstra 2016). An ideal approach for studying LAEs would be directly measuring their physical properties from observation (e.g., Dey et al. 1998; Rhoads et al. 2000; Gawiser et al. 2007). However, since most of LAEs are observed at high redshift ( $z \gtrsim 2$ , e.g., Song et al. 2014; Shibuya et al. 2019, and references therein), directly observing them has been challenging mainly due to their observed

faintness associated with redshift and the intervening intergalactic medium absorption along the line of sight. In this regard, an alternative approach for studying high- $z$  LAEs would be studying the physical properties of local analogs of high- $z$  LAEs such as GPs (e.g., Izotov et al. 2011; Yang et al. 2016, 2017).

Morphologically, it has been reported that LAEs are typically “compact,” often with multiple clumps in the rest-frame UV continuum (i.e., the effective radius  $R_{\text{eff}} \lesssim 1.5 \text{ kpc}$ ) over a wide range of redshift  $0 \lesssim z \lesssim 6$  (e.g., Bond et al. 2009; Malhotra et al. 2012; Jiang et al. 2013; Paulino-Afonso et al. 2018; Ritondale et al. 2019; Shibuya et al. 2019, and references therein). While there is an overall consensus regarding the compact and clumpy morphologies of most of the LAEs studied, it does not seem entirely clear how these compact morphologies could be related to the observed Ly $\alpha$  profiles—and more fundamentally, whether the compact/clumpy morphology of Ly $\alpha$ -emitting galaxies is one of the important physical conditions that makes a galaxy a Ly $\alpha$ -emitting galaxy (e.g., Malhotra et al. 2012; Izotov et al. 2018a).

In this context, we investigate the central UV photometric properties of LAEs and continuum-selected Lyman Break Galaxy Analogs (LBAs), and the associations with the observed Ly $\alpha$  line properties based on GPs and local LBAs (i.e., Heckman et al. 2005). We utilize Cosmic Origins Spectrograph near-ultraviolet (COS/NUV) acquisition images from the *Hubble Space Telescope* (*HST*) and the measured Ly $\alpha$  properties from the literature (i.e., Alexandroff et al. 2015; Yang et al. 2017, hereafter Y17). The physical proximity of our sample GPs and LBAs (i.e.,  $0.1 \lesssim z \lesssim 0.35$ ) and the high angular resolution (i.e.,  $0.0235 \text{ arcsec pixel}^{-1}$ ) of the COS/NUV images are suitable for studying the spatially resolved central region properties of GPs and LBAs.

Section 2 describes our galaxy sample and the central star-formation intensity (SFI) measurements. In Section 3, we present

our results. In Section 4, we discuss the implications of these results and summarize our primary conclusions. Throughout this paper, we adopt the AB magnitude system and the  $\Lambda$ CDM cosmology of  $(H_0, \Omega_m, \Omega_\Lambda) = (70 \text{ km s}^{-1} \text{ Mpc}^{-1}, 0.3, 0.7)$ .

## 2. Samples and Data Analysis

### 2.1. GP and LBA Sample

Our GP sample is drawn from the 43 galaxies presented in Y17. As described in that paper, all of the galaxies have been observed with *HST*/COS spectroscopy and the associated NUV imaging through the COS acquisition mode ACQ/IMAGE with MIRRORA except for two galaxies (GP ID 0021+0052 and 0938+5428) that have been observed with the MIRRORB configuration. We adopt additional information (e.g., GP ID, equivalent width of the Ly $\alpha$  line EW(Ly $\alpha$ ), Ly $\alpha$  escape fraction  $f_{\text{esc}}^{\text{Ly}\alpha}$ , and  $E(B - V)$ ) for our sample GP galaxies from Y17. Among the 43 galaxies, we exclude the two galaxies observed with the MIRRORB configuration in this study. We additionally exclude another galaxy (GP ID 0747+2336) because the galaxy has no Ly $\alpha$  emission line detected in the COS spectroscopy observation (see Y17 for details). Therefore, our final GP sample consists of 40 GPs.

The LBA sample is drawn from 21 galaxies analyzed by Alexandroff et al. (2015). From the 21 galaxies, we only selected galaxies observed with the MIRRORA configuration, leaving 15 galaxies. LBA ID, galaxy stellar mass, and EW(Ly $\alpha$ ) are adopted from Alexandroff et al. (2015).  $E(B - V)$  value for the Milky Way extinction is obtained from the NASA/IPAC Galactic Dust Reddening and Extinction tool. H $\alpha$  and H $\beta$  fluxes for the Balmer decrement method to derive an internal extinction correction in Section 2.3 are obtained from the MPA-JHU catalog (Brinchmann et al. 2004; Tremonti et al. 2004). We also note that 5 of the 15 LBA sample have been classified as GPs in Y17 (i.e., GP (LBA) ID 0055-0021 (J0055), 0926+4428 (J0926), 1025+3622 (J1025), 1428+1653 (J1428), and 1429+0643 (J1429)), and thus were already included in the 40 sample GPs. Therefore, the net increase in sample size is 10 additional objects classified as LBAs but not GPs. We note that any statistics quoted for the LBA sample include all 15 LBAs (both the 10 “pure” LBAs and the five overlap objects.)

For this combined sample of GPs and LBAs we use of the COS/NUV images to derive their central UV photometric properties. The exposure time of the images is typically greater than 100 s. The pivot wavelength of the observed NUV filter is 2319.7 Å.

### 2.2. Deconvolution and Segmentation Maps

We derive segmentation maps of individual galaxies from the NUV images using an approach based on Haar wavelet decomposition. In order to compare the central properties of the entire sample without bias from redshift-dependent resolution effects, we first deconvolved raw NUV images of galaxies with the COS/NUV point-spread function (PSF) image of star P330E taken during the *HST* program 11473.<sup>4</sup> Specifically, we utilized the Python-based Richardson–Lucy deconvolution package<sup>5</sup> to perform the deconvolution.

We then proceeded with a Haar wavelet decomposition, which represents the galaxy image as a weighted sum of (mutually orthogonal) 2D boxcar functions. The denoising procedure discards terms in that sum whose coefficients are not significantly different from zero, given the noise in the data. Our Haar denoising procedure<sup>6</sup> is a 2D generalization of the 1D TIPSH algorithm that Kolaczyk (1997) originally developed for modeling transient light curves.

We also estimated the sky background and subtracted from the processed (i.e., PSF-deconvolved and Haar wavelet denoised) COS/NUV images. The sky is measured by taking the average background values from the four  $50 \times 50$  pixel corner regions of the  $200 \times 200$  pixel ( $4''.7 \times 4''.7$ ) galaxy images.

We then apply the Petrosian (1976) method to the processed and sky-subtracted images to derive the galaxy segmentation maps. The Petrosian method identifies the central region of a galaxy by defining a local surface brightness threshold  $I_{\text{thresh}}$  such that  $I_{\text{thresh}} = \eta \times \bar{I}(I > I_{\text{thresh}})$ . (That is, the threshold surface brightness is a factor of  $\eta$  below the average surface brightness enclosed within a contour having surface brightness  $I_{\text{thresh}}$ . While  $I_{\text{thresh}}$  is implicitly defined, it is nevertheless a uniquely defined quantity for surface brightness profiles where both local surface brightness and total luminosity remain finite, as physics demands of real galaxies.) The  $I_{\text{thresh}}$  that satisfies the above Petrosian equation is found by sorting image pixels in descending surface brightness order, and thus the associated contour with  $I_{\text{thresh}}$  is not in general circular. This method has the advantages of being independent of the redshift of a galaxy, and relatively insensitive to dust reddening. We adopt  $\eta = 0.2$ , which is widely used for deriving galaxy segmentation maps (e.g., Shimasaku et al. 2001). The derived segmentation maps of galaxies are used for measuring the total bolometric luminosity ( $L_{\text{bol, total}}$ ) to compare with the central SFI in Section 3.1.

### 2.3. SFI Measurements from the Central 250 pc Region

We measure the SFI (star formation rate per unit area which is equivalent to star formation rate surface density; SFRD) from the central region of galaxies based on the UV surface brightness in the processed COS/NUV images described in Section 2.2. Our approach is similar to that employed in Meurer et al. (1997), Hathi et al. (2008), and Malhotra et al. (2012).

We first apply extinction corrections and  $k$ -correction to estimate the intrinsic UV continuum flux measured at the same rest-frame wavelength for each galaxy. We apply the Milky Way extinction correction following the method of Fitzpatrick & Massa (1990) and Fitzpatrick (1999). We also perform an internal extinction correction adopting the Balmer decrement method and the extinction law from Calzetti et al. (2000). The  $k$ -correction is performed with respect to the mean rest-frame wavelength of 1877.15 Å in the GP sample. We adopt the intrinsic UV slope of  $-2$  for typical starburst galaxies (e.g., Hathi et al. 2008; Malhotra et al. 2012). The galaxy center is set as the brightest pixel in the extinction and  $k$ -correction processed NUV images.

We then resample each image to a common pixel scale of  $10 \text{ pc pixel}^{-1}$ , using the IRAF “magnify” task with a redshift-dependent magnification factor. At this point, the images of our different sample galaxies have been processed to compensate

<sup>4</sup> [http://www.stsci.edu/hst/cos/documents/isrs/ISR2010\\_10.pdf](http://www.stsci.edu/hst/cos/documents/isrs/ISR2010_10.pdf)

<sup>5</sup> [https://scikit-image.org/docs/dev/api/skimage.restoration.html#skimage.restoration.richardson\\_lucy](https://scikit-image.org/docs/dev/api/skimage.restoration.html#skimage.restoration.richardson_lucy)

<sup>6</sup> [http://butler.lab.asu.edu/wavelet\\_denoising](http://butler.lab.asu.edu/wavelet_denoising)

for nonuniform properties introduced by distance (PSF deconvolution; pixel resampling), redshift ( $k$ -correction), and extinction (both foreground and internal).

We then measure the UV luminosity from the central  $250 \times 250$  pc region ( $L_{\text{bol},250 \text{ pc}}$  in the unit of  $L_{\odot}$ ) together with the associated central SFI ( $S_{250 \text{ pc}}$  in the unit of  $L_{\odot} \text{ kpc}^{-2}$ ), by directly summing up the flux from  $25 \times 25$  resampled pixels. We adopt the solar bolometric magnitude of 4.74 (Bessell et al. 1998) and the UV to bolometric luminosity ratio ( $L_{\text{UV}}/L_{\text{bol}}$ ) of 0.33 for typical starbursts (e.g., Meurer et al. 1997; Hathi et al. 2008). We also convert luminosities ( $L_{\odot}$ ) into equivalent star formation rates ( $M_{\odot} \text{ yr}^{-1}$ ) by using the scale factor  $L_{\text{bol}}/(4.5 \times 10^9 L_{\odot}) = \text{SFR}/(1 M_{\odot} \text{ yr}^{-1})$ . This factor is derived by Meurer et al. (1997) based on starburst population modeling with a solar metallicity and a Salpeter (1955) initial mass function with lower and upper limit masses of  $0.1 M_{\odot}$  and  $100 M_{\odot}$ , respectively.

Examples of raw NUV images, the deconvolved images, the Haar wavelet denoised images, and the derived segmentation maps of some sample galaxies are shown in Figure 1. Also, the measured  $S_{250 \text{ pc}}$  and  $L_{\text{bol},\text{total}}$  are provided in Table 1.

### 3. Results

#### 3.1. Equivalent Width and Escape Fraction of $\text{Ly}\alpha$ Emission versus the Central SFI

We now investigate whether the  $\text{Ly}\alpha$  properties of GPs and LBAs are related to their central SFI.<sup>7</sup> Figure 2 shows the relations between  $\text{EW}(\text{Ly}\alpha)$ ,  $f_{\text{esc}}^{\text{Ly}\alpha}$ , and  $S_{250 \text{ pc}}$ . First of all, the measured  $\log(S_{250 \text{ pc}}/M_{\odot} \text{ yr}^{-1} \text{ kpc}^{-2})$  for 40 sample GPs ranges from  $\sim 0.37$  to  $\sim 1.66$ , with a mean  $\log(S_{250 \text{ pc}}/M_{\odot} \text{ yr}^{-1} \text{ kpc}^{-2})$  of 1.17. Compared to approximately two orders of magnitude distributions of  $\text{EW}(\text{Ly}\alpha)$  and  $f_{\text{esc}}^{\text{Ly}\alpha}$  of sample GPs, the distribution of their  $S_{250 \text{ pc}}$  is narrower by an order of magnitude. It has a standard deviation of 0.266 dex, which corresponds to a factor of  $\sim 1.85$ . For the 15 sample LBAs (that is, including the 5 LBAs also classified as GPs), their measured  $\log(S_{250 \text{ pc}}/M_{\odot} \text{ yr}^{-1} \text{ kpc}^{-2})$  is typically larger than that of GPs. The mean  $\log(S_{250 \text{ pc}}/M_{\odot} \text{ yr}^{-1} \text{ kpc}^{-2})$  is 1.45 with a standard deviation of 0.271 dex.

We find no significant correlations of either  $\text{EW}(\text{Ly}\alpha)$  (a) or  $f_{\text{esc}}^{\text{Ly}\alpha}$  (b) with  $S_{250 \text{ pc}}$ , at least for our sample of GPs (i.e., the diamond symbol in the figure) with their relatively narrow dynamic range of  $S_{250 \text{ pc}}$ . The associated Spearman correlation coefficients (hereafter,  $r_s$ ) ( $p$ -value) with  $\text{EW}(\text{Ly}\alpha)$  and  $f_{\text{esc}}^{\text{Ly}\alpha}$  are only 0.074 (0.7) and  $-0.027$  (0.9), respectively. For comparison, the total bolometric luminosity  $L_{\text{bol},\text{total}}$  shows weak and statistically insignificant anticorrelations with  $\text{EW}(\text{Ly}\alpha)$  and  $f_{\text{esc}}^{\text{Ly}\alpha}$ , with the associated  $r_s$  values ( $p$ -values) of  $-0.206$  (0.2) and  $-0.230$  (0.2), respectively. Even with the inclusion of LBAs, the correlation between  $\text{EW}(\text{Ly}\alpha)$  and  $S_{250 \text{ pc}}$  in (a) does not seem significant, with the associated  $r_s$  ( $p$ -value) of  $-0.079$  (0.6).

We also mark the five confirmed  $\text{LyC}$  leakers from Izotov et al. (2016) among our sample GPs in the figure (i.e., the red-filled diamonds). The  $S_{250 \text{ pc}}$  that we derived for these  $\text{LyC}$  leakers using NUV-continuum flux is in broad agreement with that derived using  $\text{H}\beta$  luminosity and the measured NUV-continuum size (i.e., in the unit of scalelength) in

<sup>7</sup> We note that our analysis with our sample LBAs is limited to their  $\text{EW}(\text{Ly}\alpha)$ , since there is no measured  $f_{\text{esc}}^{\text{Ly}\alpha}$  for our sample LBAs from the literature.

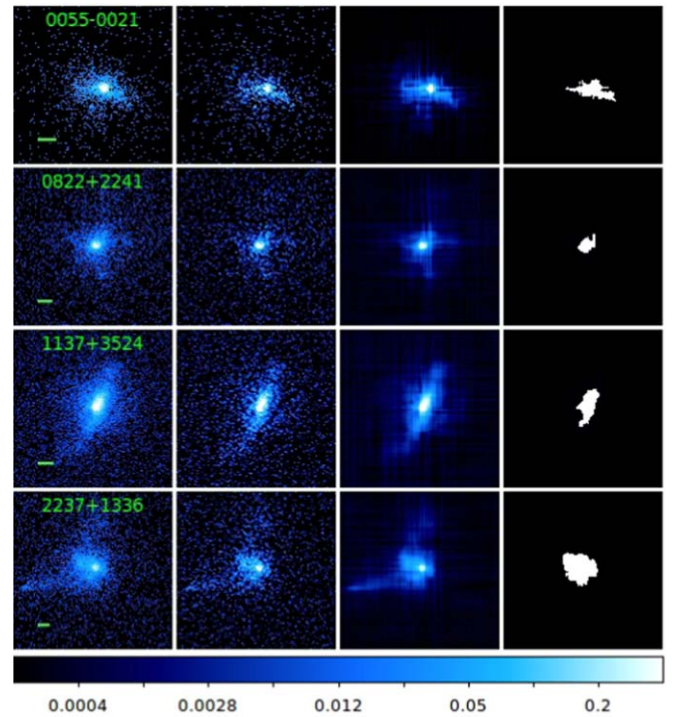


**Figure 1.** Examples of COS/NUV images of some Green Pea (GP) samples. Each row shows an individual GP. From left to right, the raw NUV image, the PSF-deconvolved image, the Haar-denoised image, and the segmentation map are displayed, respectively. All images are  $3'' \times 3''$  sized. GP ID is marked top middle and a green bar indicates 1 kpc in the raw NUV image. The color bar at the bottom represents flux in the unit of  $\text{count s}^{-1}$ .

Izotov et al. (2016), matching within a factor of  $\sim 2$ , except for one galaxy (GP ID 1333+6246) that shows a factor of  $\sim 3$  difference between the studies.

#### 3.2. Examining Specific SFI

The sSFR, defined as SFR normalized by stellar mass, is a powerful summary statistic for the level of star formation in galaxies (e.g., Whitaker et al. 2012; Kim et al. 2018). Since the power available to drive galactic winds increases with increasing star formation, while the escape velocity for such winds increases with stellar mass, it is reasonable to expect galactic-scale outflows to be more common and stronger where sSFR is high. Very actively star-forming galaxies like GPs and higher redshift  $\text{Ly}\alpha$  emitters commonly have  $\text{sSFR} \gtrsim 10^{-8} \text{ yr}^{-1}$ , implying stellar mass doubling times of  $< 10^8 \text{ yr}$  (e.g., Cardamone et al. 2009; Izotov et al. 2011; Finkelstein et al. 2015; Yang et al. 2017; Jiang et al. 2019).

Next, therefore, we examine the dependences of  $\text{EW}(\text{Ly}\alpha)$ ,  $f_{\text{esc}}^{\text{Ly}\alpha}$ , and  $S_{250 \text{ pc}}$  on both sSFR and also the specific star-formation intensity (sSFI), which we define as the SFI divided by total stellar mass. LAEs, including GPs, typically have low stellar mass ( $8 \lesssim \log(M_{\text{star}}/M_{\odot}) \lesssim 10$ ; e.g., Gawiser et al. 2007; Pirzkal et al. 2007; Y17), and show an anticorrelation between stellar mass and  $\text{EW}(\text{Ly}\alpha)$  (e.g., Marchi et al. 2019). This provides a further empirical motivation to investigate the effect of stellar mass on the observed trends between  $\text{EW}(\text{Ly}\alpha)$ ,  $f_{\text{esc}}^{\text{Ly}\alpha}$ , and  $S_{250 \text{ pc}}$ . Figure 3 again plots both  $\text{EW}(\text{Ly}\alpha)$  and  $f_{\text{esc}}^{\text{Ly}\alpha}$ , but now as functions of  $S_{250 \text{ pc}}$  divided by stellar mass ( $\log S_{250 \text{ pc}}/M_{\text{star}}$ ). For our sample GPs, we find that both  $\text{EW}(\text{Ly}\alpha)$  and  $f_{\text{esc}}^{\text{Ly}\alpha}$  show significant positive

**Table 1**  
The Measured  $S_{250\text{ pc}}$  and  $L_{\text{bol,total}}$ , and Adopted EW(Ly $\alpha$ ) and  $f_{\text{esc}}^{\text{Ly}\alpha}$  of Sample Galaxies

Green Pea ID <sup>a</sup>	SDSS ObjID <sup>b</sup>	$\log S_{250\text{ pc}}^{\text{c,d}}$ ( $L_{\odot} \text{ kpc}^{-2}$ )	$\log(\text{SFI})^{\text{c,e}}$ ( $M_{\odot} \text{ yr}^{-1} \text{ kpc}^{-2}$ )	$\log L_{\text{bol,total}}^{\text{c,f}}$ ( $L_{\odot}$ )	$\log(\text{SFR})^{\text{c,g}}$ ( $M_{\odot} \text{ yr}^{-1}$ )	EW(Ly $\alpha$ ) <sup>h</sup> ( $\text{\AA}$ )	$f_{\text{esc}}^{\text{Ly}\alpha}$ <sup>i</sup>
0055-0021 <sup>j</sup>	1237663783666581565	11.099 ± 0.100	1.445 ± 0.100	10.411 ± 0.171	0.757 ± 0.171	3.20	0.005
0303-0759	1237652900231053501	10.876 ± 0.025	1.223 ± 0.025	10.124 ± 0.054	0.470 ± 0.054	14.17	0.098
0339-0725	1237649961383493869	10.851 ± 0.050	1.198 ± 0.050	10.808 ± 0.083	1.155 ± 0.083	6.74	0.016
0749+3337	1237674366992646574	10.901 ± 0.054	1.247 ± 0.054	10.962 ± 0.105	1.310 ± 0.105	8.86	0.010
0751+1638	1237673807042708368	10.393 ± 0.075	0.740 ± 0.075	10.149 ± 0.149	0.496 ± 0.149	15.77	0.043
0805+0925	123766729656905788	10.725 ± 0.077	1.071 ± 0.077	10.582 ± 0.141	0.929 ± 0.141	9.20	0.009
0815+2156	1237664668421849521	10.690 ± 0.017	1.036 ± 0.017	9.793 ± 0.035	0.139 ± 0.035	82.15	0.327
0822+2241	1237664092897083648	11.054 ± 0.038	1.401 ± 0.038	10.401 ± 0.076	0.784 ± 0.076	51.62	0.037
0911+1831	1237667429018697946	11.197 ± 0.017	1.543 ± 0.017	10.621 ± 0.033	0.968 ± 0.033	56.53	0.177
0917+3152	1237661382232768711	11.311 ± 0.032	1.658 ± 0.032	10.760 ± 0.045	1.107 ± 0.045	37.97	0.169
0925+1403 <sup>k</sup>	1237671262812897597	11.042 ± 0.014	1.389 ± 0.014	10.500 ± 0.028	0.846 ± 0.028	90.01	0.186
0926+4428 <sup>j</sup>	1237657630590107652	10.915 ± 0.080	1.262 ± 0.080	10.328 ± 0.115	0.675 ± 0.115	47.85	0.287
0927+1740	1237667536393142625	10.489 ± 0.071	0.835 ± 0.071	10.479 ± 0.126	0.826 ± 0.126	7.20	0.013
1009+2916	1237665126921011548	10.470 ± 0.047	0.817 ± 0.047	9.884 ± 0.078	0.230 ± 0.078	69.54	0.373
1018+4106	1237661851459584247	10.557 ± 0.045	0.904 ± 0.045	10.101 ± 0.104	0.457 ± 0.104	33.05	0.059
1025+3622 <sup>j</sup>	1237664668435677291	10.780 ± 0.048	1.126 ± 0.048	10.433 ± 0.096	0.779 ± 0.096	26.27	0.154
1032+2717	1237667211592794251	10.408 ± 0.064	0.755 ± 0.064	9.990 ± 0.108	0.337 ± 0.108	5.50	0.009
1054+5238	1237658801495474207	11.045 ± 0.034	1.392 ± 0.034	10.705 ± 0.053	1.052 ± 0.053	17.65	0.112
1122+6154	1237655464839479591	10.866 ± 0.033	1.213 ± 0.033	9.957 ± 0.057	0.304 ± 0.057	59.95	0.187
1133+6514	1237651067351073064	10.507 ± 0.030	0.854 ± 0.030	10.334 ± 0.060	0.681 ± 0.060	42.30	0.422
1137+3524	1237665129613885585	10.903 ± 0.029	1.250 ± 0.029	10.483 ± 0.059	0.829 ± 0.059	40.45	0.157
1152+3400 <sup>k</sup>	1237665127467647162	10.961 ± 0.021	1.308 ± 0.021	10.671 ± 0.039	1.018 ± 0.039	74.45	0.287
1205+2620	1237667321644908846	10.942 ± 0.039	1.289 ± 0.039	10.422 ± 0.073	0.769 ± 0.073	3.00	0.006
1219+1526	1237661070336852109	10.897 ± 0.023	1.244 ± 0.023	10.243 ± 0.036	0.590 ± 0.036	164.55	0.702
1244+0216	1237671266571387104	10.697 ± 0.021	1.044 ± 0.021	10.558 ± 0.065	0.904 ± 0.065	46.98	0.077
1249+1234	1237661817096962164	10.749 ± 0.019	1.096 ± 0.019	10.404 ± 0.047	0.751 ± 0.047	101.82	0.412
1333+6246 <sup>k</sup>	1237651249891967264	10.538 ± 0.017	0.885 ± 0.017	10.176 ± 0.047	0.523 ± 0.047	72.34	1.180
1339+1516	1237664292084318332	10.984 ± 0.037	1.331 ± 0.037	10.091 ± 0.054	0.438 ± 0.054	44.74	0.034
1424+4217	1237661360765730849	10.724 ± 0.033	1.071 ± 0.033	10.101 ± 0.069	0.448 ± 0.069	89.53	0.290
1428+1653 <sup>j</sup>	1237668297680683015	11.192 ± 0.032	1.539 ± 0.032	10.761 ± 0.070	1.108 ± 0.070	29.07	0.106
1429+0643 <sup>j</sup>	1237662268069511204	11.045 ± 0.073	1.392 ± 0.073	10.459 ± 0.094	0.806 ± 0.094	42.75	0.123
1440+4619	1237662301362978958	11.154 ± 0.040	1.501 ± 0.040	10.815 ± 0.068	1.162 ± 0.068	33.82	0.128
1442-0209 <sup>k</sup>	1237655498671849789	11.124 ± 0.018	1.470 ± 0.018	10.416 ± 0.042	0.763 ± 0.042	134.90	0.430
1454+4528	1237662301900964026	11.118 ± 0.036	1.465 ± 0.036	10.496 ± 0.069	0.843 ± 0.069	29.95	0.061
1457+2232	1237665549967294628	10.804 ± 0.019	1.151 ± 0.019	9.987 ± 0.044	0.334 ± 0.044	5.30	0.010
1503+3644 <sup>k</sup>	1237661872417407304	10.811 ± 0.014	1.158 ± 0.014	10.262 ± 0.025	0.609 ± 0.025	106.61	0.431
1514+3852	1237661362380734819	10.876 ± 0.031	1.223 ± 0.031	10.272 ± 0.051	0.619 ± 0.051	60.00	0.698
1543+3446	1237662336790036887	10.024 ± 0.080	0.371 ± 0.080	9.654 ± 0.141	0.001 ± 0.141	5.40	0.024
1559+0841	1237662636912280219	10.628 ± 0.039	0.975 ± 0.039	9.936 ± 0.068	0.283 ± 0.068	95.96	0.735
2237+1336	1237656495641788638	10.752 ± 0.054	1.099 ± 0.054	10.758 ± 0.124	1.104 ± 0.124	15.31	0.063
<b>LBA ID<sup>l</sup></b>							
J0150	1237649918971084879	11.019 ± 0.070	1.365 ± 0.070	10.431 ± 0.145	0.778 ± 0.145	3.04	...
J0213	1237649919510446221	11.318 ± 0.073	1.665 ± 0.073	10.317 ± 0.092	0.664 ± 0.092	9.20	...
J0921	1237657242433486943	11.440 ± 0.021	1.787 ± 0.021	10.885 ± 0.041	1.232 ± 0.041	4.01	...
J2103	1237652598489153748	11.471 ± 0.134	1.818 ± 0.134	10.517 ± 0.147	0.864 ± 0.147	25.56	...
J1112	1237657591929831540	11.236 ± 0.058	1.582 ± 0.058	10.683 ± 0.082	1.030 ± 0.082	7.60	...
J1113	1237667212133728444	10.620 ± 0.033	0.966 ± 0.033	10.290 ± 0.133	0.637 ± 0.133	0.85	...
J1144	1237662225675124894	10.687 ± 0.049	1.034 ± 0.049	10.573 ± 0.109	0.919 ± 0.109	0.78	...
J1416	1237662528992378986	11.240 ± 0.094	1.587 ± 0.094	10.504 ± 0.101	0.851 ± 0.101	1.69	...
J1521	1237662264860344485	10.980 ± 0.072	1.327 ± 0.072	10.456 ± 0.095	0.802 ± 0.095	3.96	...
J1612	1237662637450592299	11.447 ± 0.071	1.794 ± 0.071	10.857 ± 0.088	1.204 ± 0.088	13.60	...

**Notes.**<sup>a</sup> GP IDs match those in Yang et al. (2017).<sup>b</sup> SDSS DR14 BestObjID.<sup>c</sup> The associated errors are flux measurement uncertainties based on photon counting statistics (i.e., Poisson statistics) and propagation of the errors during the image calibration procedures such as flat-field correction. Resulting errors are typically 0.05 dex and 0.081 dex in  $S_{250\text{ pc}}$  and  $L_{\text{bol,total}}$ , respectively. Additional sources of measurement uncertainty come from the UV-continuum extinction corrections and the  $k$ -correction described in Section 2.3. These corrections are typically 0.29 dex and 0.04 dex, respectively, with uncertainties that are considerably smaller than the corrections but still potentially significant.<sup>d</sup> The measured  $S_{250\text{ pc}}$  in the unit of  $L_{\odot} \text{ kpc}^{-2}$ . See Section 2.3 for details.<sup>e</sup> The measured SFI in the unit of  $M_{\odot} \text{ yr}^{-1} \text{ kpc}^{-2}$ , which is converted from  $L_{\odot} \text{ kpc}^{-2}$  into equivalent star formation rate surface density (SFRD). See Section 2.3 for details.<sup>f</sup> The measured  $L_{\text{bol,total}}$  in the unit of  $L_{\odot}$ . See Section 2.3 for details.<sup>g</sup> The measured star formation rate (SFR) in the unit of  $M_{\odot} \text{ yr}^{-1}$ , which is converted from  $L_{\odot}$  into the equivalent SFR. See Section 2.3 for details.<sup>h</sup> Equivalent width of Ly $\alpha$  emission line. EW(Ly $\alpha$ ) is measured in Yang et al. (2017) and Alexandroff et al. (2015) for the sample GPs and LBAs, respectively. The typical measurement uncertainties are  $\sim 15\%$  mainly dominated by the systematic error.<sup>i</sup> Ly $\alpha$  escape fraction measured in Yang et al. (2017). The typical measurement uncertainties are  $\sim 15\%$  mainly dominated by the systematic error.<sup>j</sup> GPs that are also classified as LBAs by Alexandroff et al. (2015).<sup>k</sup> Confirmed LyC leakers identified by Izotov et al. (2016).<sup>l</sup> LBA IDs match those in Alexandroff et al. (2015).

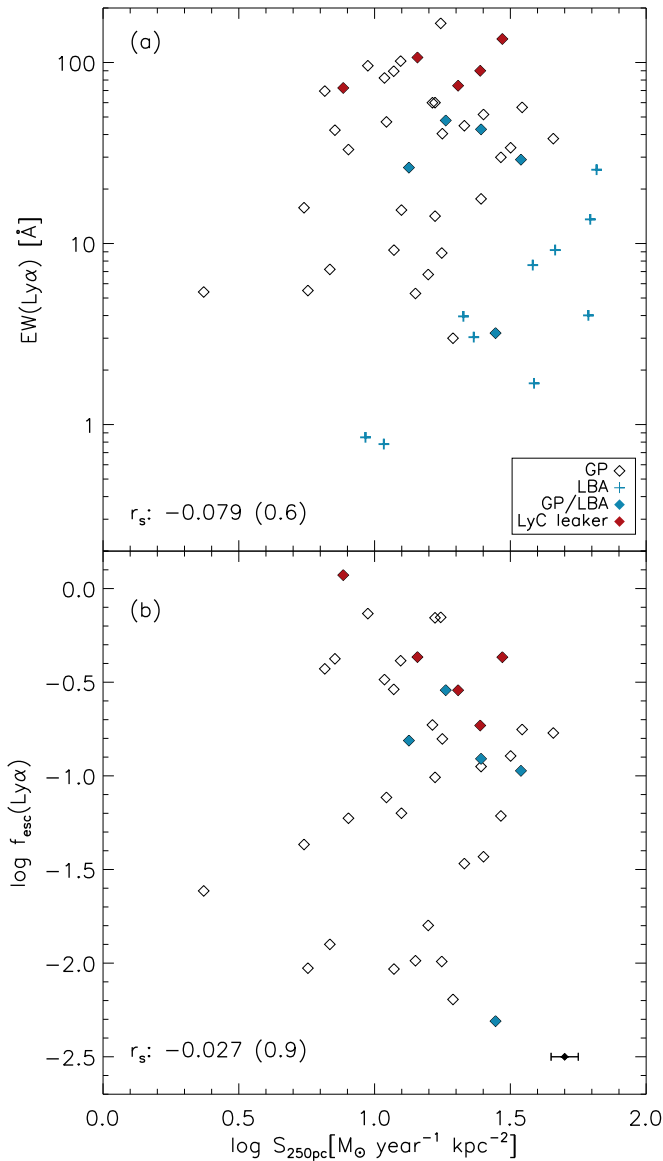


**Figure 2.**  $EW(Ly\alpha)$  (a) and  $f_{esc}^{Ly\alpha}$  (b) vs.  $S_{250 pc}$  for sample GPs and LBAs and sample GPs only, respectively. The associated  $r_s$  values ( $p$ -values) are shown in bottom left of each panel. In panel (a), the blue crosses are LBAs, while the blue-filled diamonds are the LBAs that are also classified as GPs (see Section 2.1 for details). The red-filled diamonds indicate the five confirmed LyC leakers from Izotov et al. (2016). The typical measurement error in  $S_{250 pc}$  due to photon counts and propagation of the errors during the image calibration procedures such as flat-field correction is 0.05 dex, which corresponds to 0.125 error in magnitude. The typical error is marked in the bottom right in panel (b). Also, we note that the Milky Way and internal extinction corrections and the  $k$ -correction performed in Section 2.3 typically result in 0.29 dex and 0.04 dex corrections in the measured  $\log(S_{250 pc}/M_{\odot} yr^{-1} kpc^{-2})$ , respectively. The typical measurement uncertainties of our adopted  $EW(Ly\alpha)$  and  $f_{esc}^{Ly\alpha}$  from Y17 are  $\sim 15\%$  mainly dominated by the systematic error. The similar uncertainties are applied to the measured  $EW(Ly\alpha)$  from Alexandroff et al. (2015). See the text for details.

correlations with  $\log S_{250 pc}/M_{star}$ . The correlations with  $\log S_{250 pc}/M_{star}$  are stronger than those with sSFR (which are  $r_s = 0.475$ ,  $p = 2 \times 10^{-3}$ ; and  $r_s = 0.420$ ,  $p = 7 \times 10^{-3}$ , respectively.) Moreover, when our sample LBAs are also considered in the correlation between  $EW(Ly\alpha)$  and  $\log S_{250 pc}/M_{star}$  (i.e., Figure 3(a)), the associated  $r_s$  value shows the most significant correlation coefficient of 0.702 with its  $p$ -value of  $10^{-8}$  among the ones we explored.

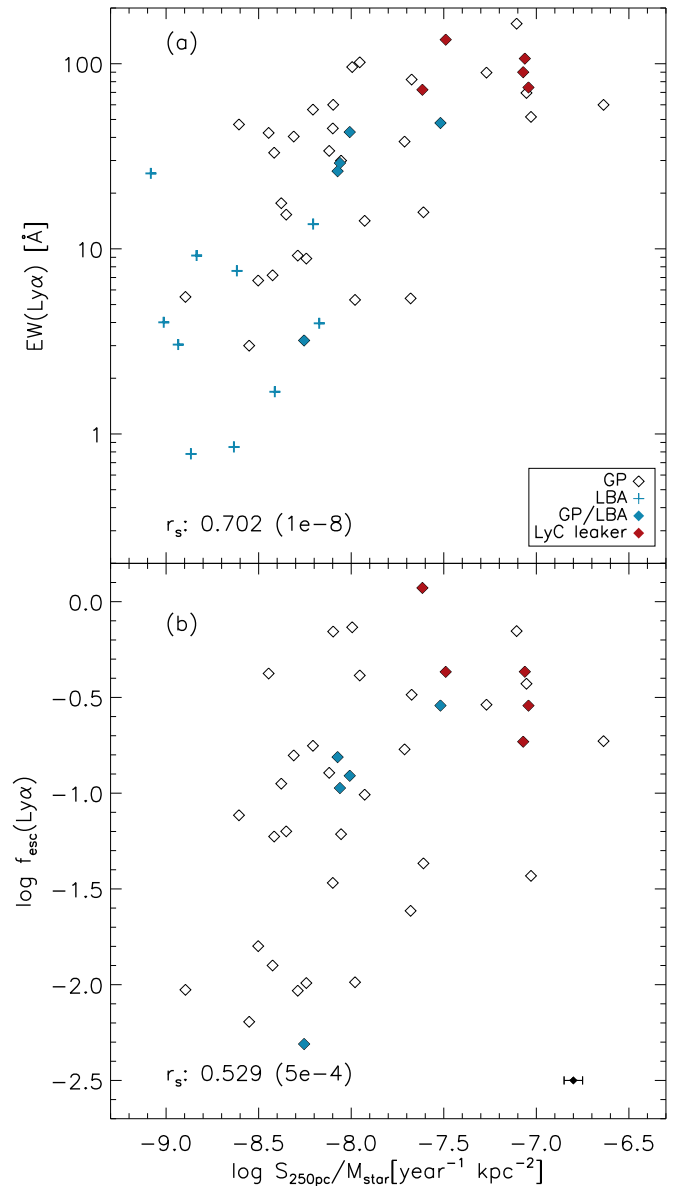


**Figure 3.** Same as Figure 2, but for against  $\log S_{250 pc}/M_{star}$  on  $x$ -axis. The more significant positive correlations of  $EW(Ly\alpha)$  and  $f_{esc}^{Ly\alpha}$  with  $\log S_{250 pc}/M_{star}$  than with  $S_{250 pc}$  are shown.

All the correlation coefficients are summarized in Table 2. As in Figure 2, the five confirmed LyC leakers are marked in the red-filled diamonds in Figure 3. In the parameter space of  $S_{250 pc}/M_{star}$ , all five LyC leakers have  $S_{250 pc}/M_{star} \gtrsim 10^{-7.7} yr^{-1} kpc^{-2}$ , larger than the median of  $10^{-8.1} yr^{-1} kpc^{-2}$  of the entire sample distribution.

#### 4. Discussion and Conclusions

In this study, we have identified a sample of GP and Lyman Break Analog galaxies, which are (respectively) some of the best local analogs of high- $z$  Ly $\alpha$  and Lyman break galaxies. Using this sample, we have measured the central UV SFI ( $S_{250 pc}$ ) and sSFI  $S_{250 pc}/M_{star}$ , and investigated the correlations between these two quantities and Ly $\alpha$  line strength, as characterized by  $EW(Ly\alpha)$  and  $f_{esc}^{Ly\alpha}$ . We summarize our primary results and conclusions below.

**Table 2**  
The Spearman Correlation Coefficients Between Parameters, and the Associated Probability Values

Parameter	EW(Ly $\alpha$ )		$f_{\text{esc}}^{\text{Ly}\alpha}$	
	$r_s$	$p$	$r_s$	$p$
GP only				
SFI $\equiv S_{250 \text{ pc}}$	0.074	0.7	-0.027	0.9
$L_{\text{bol, total}}$	-0.206	0.2	-0.229	0.2
sSFR $\equiv \text{SFR}/M_{\text{star}}$	0.475	$2 \times 10^{-3}$	0.420	$7 \times 10^{-3}$
$1/M_{\text{star}}$	0.544	$3 \times 10^{-4}$	0.503	$1 \times 10^{-3}$
sSFI $\equiv S_{250 \text{ pc}}/M_{\text{star}}$	0.626	$2 \times 10^{-5}$	0.529	$5 \times 10^{-4}$
GP+LBA				
SFI $\equiv S_{250 \text{ pc}}$	-0.079	0.6	...	...
$L_{\text{bol, total}}$	-0.272	0.06	...	...
sSFR $\equiv \text{SFR}/M_{\text{star}}$	0.617	$2 \times 10^{-6}$	...	...
$1/M_{\text{star}}$	0.645	$4 \times 10^{-7}$	...	...
sSFI $\equiv S_{250 \text{ pc}}/M_{\text{star}}$	0.702	$1 \times 10^{-8}$	...	...

First, the central UV SFI of GPs and LBAs is approximately three orders of magnitude larger than typical for normal star-forming galaxies (e.g., Kennicutt 1998). Moreover, this SFI has a relatively narrow distribution, with  $\sigma \sim 0.27$  dex. And, the typical SFI for LBAs is about double that for GPs. (Specifically, the mean  $S_{250 \text{ pc}}$  is  $\sim 28 M_{\odot} \text{ yr}^{-1} \text{ kpc}^{-2}$  for LBAs, and  $15 M_{\odot} \text{ yr}^{-1} \text{ kpc}^{-2}$  for GPs.)

Such high SFI may blow significant holes in the ISM, where the HI column density ( $N_{\text{HI}}$ ) becomes low enough that Ly $\alpha$  photons escape more easily, as some numerical simulations on star formation and the escape of ionizing photons in disk galaxies demonstrated (e.g., Wood & Loeb 2000; Fujita et al. 2003). We note that most Ly $\alpha$ -emitting galaxies have compact morphological properties (e.g., Malhotra et al. 2012; Alexandroff et al. 2015; Verhamme et al. 2017; Izotov et al. 2018a; Ritondale et al. 2019), and that their small sizes allow moderate star formation to produce the comparatively high SFI ( $\gtrsim 0.1 M_{\odot} \text{ yr}^{-1} \text{ kpc}^{-2}$ , Heckman 2001; Izotov et al. 2016) needed for this mechanism.

High SFI is linked to high central pressure  $P_0$ . This pressure is most likely dominated by contributions from stellar winds and (possibly) supernovae feedback from the central starburst regions, and may drive galactic outflows (e.g., Heckman et al. 2015; Heckman & Borthakur 2016). (Note, however, that intense star formation in nascent massive star clusters can generate high ambient pressure, but under some conditions may also lead to radiative cooling that reduces the resulting feedback e.g., Silich & Tenorio-Tagle 2018.) Indeed, all of our sample GPs and LBAs have SFI  $> 0.1 M_{\odot} \text{ yr}^{-1} \text{ kpc}^{-2}$ , which is a suggested SFI threshold for galactic-scale outflows (i.e., Heckman 2002). Adopting the relationship between the effective surface brightness  $S_{\text{eff}}$  and  $P_0$  of  $S_{\text{eff}}/10^{11} L_{\odot} \text{ kpc}^{-2} = P_0/1.63 \times 10^{-9} \text{ dy cm}^{-2}$  (which Meurer et al. 1997 derived from a starburst population model), the  $S_{250 \text{ pc}}$  distribution of our GP and LBA samples corresponds to the  $P_0$  range of  $10^{6.1} \text{ K cm}^{-3} \lesssim P_0/k_B \lesssim 10^{7.54} \text{ K cm}^{-3}$ , with a median  $P_0/k_B$  of  $10^{6.97} \text{ K cm}^{-3}$ , where  $k_B$  is the Boltzmann constant. Although the details and uncertainties should be considered, the  $P_0/k_B$  distribution derived using  $S_{250 \text{ pc}}$  is largely consistent with the gas pressures derived using

optical emission lines in a sample of GPs and LBAs (i.e., Jiang et al. 2019).

However, high SFI alone does not guarantee high Ly $\alpha$  photon escape, since the direct comparisons between  $S_{250 \text{ pc}}$ , EW(Ly $\alpha$ ), and  $f_{\text{esc}}^{\text{Ly}\alpha}$  do not show significant positive correlations. In particular, our sample LBAs show larger  $S_{250 \text{ pc}}$  than our sample GPs do, but do not necessarily show larger EW(Ly $\alpha$ ) (i.e., Figure 2). The absence of significant correlations between EW(Ly $\alpha$ ) or  $f_{\text{esc}}^{\text{Ly}\alpha}$  and  $S_{250 \text{ pc}}$  suggests that additional physical properties beyond high SFI alone must play a large role in Ly $\alpha$  photon escape. These could include low gas density associated with the ISM geometry, low stellar mass, low gas-phase metallicity, and so on (e.g., Gawiser et al. 2007; Shibuya et al. 2014; Song et al. 2014; Y17).

The strongest correlations in our study are of EW(Ly $\alpha$ ) and  $f_{\text{esc}}^{\text{Ly}\alpha}$  with sSFI  $\equiv S_{250 \text{ pc}}/M_{\text{star}}$  (Figure 3 and Table 2), and not with  $S_{250 \text{ pc}}$  alone. This suggests that stellar mass (or related galaxy properties) plays a role in Ly $\alpha$  escape, such that galaxies with lower stellar masses have higher Ly $\alpha$  escape for any particular value of  $S_{250 \text{ pc}}$ . The correlations of EW(Ly $\alpha$ ) with  $S_{250 \text{ pc}}/M_{\text{star}}$  ( $r_s = 0.626$ ,  $p = 2 \times 10^{-5}$ ) and  $f_{\text{esc}}^{\text{Ly}\alpha}$  with  $S_{250 \text{ pc}}/M_{\text{star}}$  ( $r_s = 0.529$ ,  $p = 5 \times 10^{-4}$ ) are stronger than the corresponding correlations with  $1/M_{\text{star}}$  alone ( $r_s = 0.544$ ,  $p = 3 \times 10^{-4}$ ; and  $r_s = 0.503$ ,  $p = 1 \times 10^{-3}$ ). They are likewise stronger than the correlations with sSFR, as examined in Section 3.2.

The correlation between EW(Ly $\alpha$ ) and sSFI becomes even stronger when we add the LBAs to the sample, with  $r_s = 0.702$  and  $p = 10^{-8}$ .

We suggest Ly $\alpha$  escape in galaxies that have high sSFI results from an interstellar medium with holes in the neutral hydrogen distribution, and/or outflow of neutral hydrogen (with consequent reduction of resonant scattering optical depth). Such ISM geometry and kinematics would be produced by the combination of high pressure in regions of high SFI, which provides a driving force for outflows that clear neutral hydrogen; and low mass, which results in shallow gravitational potentials and makes it easier for winds to effectively remove material from the neighborhood of the star formation. There is a metallicity dependence in the conversion from H $\alpha$  luminosity to SFR, but over the full metallicity range of our sample ( $7.7 \lesssim 12 + \log(\text{O}/\text{H}) \lesssim 8.5$ ) this conversion factor changes only 0.1 dex (see Figure 6 of Lee et al. 2009). This is insignificant compared to the 2.5 dex spread we observe in sSFI.

The importance of sSFI in UV photon escape is further demonstrated by a progression in measured sSFI between LyC leakers, GPs, and LBAs. LyC leakers typically show the highest sSFI, GPs the next, and LBAs the lowest (i.e., Figure 3(a)). Both LyC and Ly $\alpha$  escape are enabled by low HI column densities, but LyC escape tends to require lower columns than Ly $\alpha$  escape, especially given that resonant scattering effects may enable Ly $\alpha$  to escape for a wider range of geometries (e.g., Neufeld 1991).

In conclusion, we have examined the relation between Ly $\alpha$  emission and multiple tracers of star formation activity. We find that both high SFI (defined as star formation rate per area) and high sSFR (star formation rate per unit stellar mass) are general properties of GPs and LBAs, distinguishing them from the broader population of star-forming galaxies. But beyond that, we have demonstrated that the sSFI (defined as SFI per unit stellar mass) is the most powerful predictor of Ly $\alpha$

emission. This is likely because channels of low H I opacity are more easily cleared in galaxies with high sSFI, due to the interplay between SFI that drives galactic winds and gravitational potential that impedes them.

We thank the anonymous referee for constructive comments that improved the manuscript. K.K. thanks Gerhardt Meurer, Sanchayeeta Borthakur, and Rolf Jansen for helpful discussions. This work has been supported by HST-GO-14201 and HST-GO-15614 from STScI, which is operated by the Association of Universities for Research in Astronomy, Inc., for NASA under contract NAS 5-26555; and by NASA through Award No. NNG16PJ33C.

### ORCID iDs

Keunho Kim  <https://orcid.org/0000-0001-6505-0293>  
 Sangeeta Malhotra  <https://orcid.org/0000-0002-9226-5350>  
 James E. Rhoads  <https://orcid.org/0000-0002-1501-454X>  
 Nathaniel R. Butler  <https://orcid.org/0000-0002-9110-6673>  
 Huan Yang  <https://orcid.org/0000-0003-2260-7420>

### References

- Ahn, S.-H., Lee, H.-W., & Lee, H. M. 2003, *MNRAS*, **340**, 863  
 Alexandroff, R. M., Heckman, T. M., Borthakur, S., et al. 2015, *ApJ*, **810**, 104  
 Amorín, R. O., Pérez-Montero, E., & Vilchez, J. M. 2010, *ApJL*, **715**, L128  
 Bessell, M. S., Castelli, F., & Plez, B. 1998, *A&A*, **333**, 231  
 Bond, N. A., Gawiser, E., Gronwall, C., et al. 2009, *ApJ*, **705**, 639  
 Brinchmann, J., Charlot, S., White, S. D. M., et al. 2004, *MNRAS*, **351**, 1151  
 Calzetti, D., Armus, L., Bohlin, R. C., et al. 2000, *ApJ*, **533**, 682  
 Cardamone, C., Schawinski, K., Sarzi, M., et al. 2009, *MNRAS*, **399**, 1191  
 de Barros, S., Vanzella, E., Amorín, R., et al. 2016, *A&A*, **585**, A51  
 Dey, A., Spinrad, H., Stern, D., et al. 1998, *ApJL*, **498**, L93  
 Finkelstein, K. D., Finkelstein, S. L., Tilvi, V., et al. 2015, *ApJ*, **813**, 78  
 Fitzpatrick, E. L. 1999, *PASP*, **111**, 63  
 Fitzpatrick, E. L., & Massa, D. 1990, *ApJS*, **72**, 163  
 Fujita, A., Martin, C. L., Mac Low, M.-M., & Abel, T. 2003, *ApJ*, **599**, 50  
 Gawiser, E., Francke, H., Lai, K., et al. 2007, *ApJ*, **671**, 278  
 Gronke, M., & Dijkstra, M. 2016, *ApJ*, **826**, 14  
 Hathi, N. P., Malhotra, S., & Rhoads, J. E. 2008, *ApJ*, **673**, 686  
 Heckman, T. M. 2001, in ASP Conf. Proc. 240, Gas and Galaxy Evolution, ed. J. E. Hibbard, M. Rupen, & J. H. van Gorkom (San Francisco, CA: ASP), 345  
 Heckman, T. M. 2002, in ASP Conf. Proc. 254, Extragalactic Gas at Low Redshift, ed. J. S. Mulchaey & J. Stocke (San Francisco, CA: ASP), 292  
 Heckman, T. M., Alexandroff, R. M., Borthakur, S., et al. 2015, *ApJ*, **809**, 147  
 Heckman, T. M., & Borthakur, S. 2016, *ApJ*, **822**, 9  
 Heckman, T. M., Hoopes, C. G., Seibert, M., et al. 2005, *ApJL*, **619**, L35  
 Henry, A., Scarlata, C., Martin, C. L., et al. 2015, *ApJ*, **809**, 19  
 Izotov, Y. I., Guseva, N. G., & Thuan, T. X. 2011, *ApJ*, **728**, 161  
 Izotov, Y. I., Schaerer, D., Thuan, T. X., et al. 2016, *MNRAS*, **461**, 3683  
 Izotov, Y. I., Schaerer, D., Worseck, G., et al. 2018a, *MNRAS*, **474**, 4514  
 Izotov, Y. I., Worseck, G., Schaerer, D., et al. 2018b, *MNRAS*, **478**, 4851  
 Jaskot, A. E., & Oey, M. S. 2013, *ApJ*, **766**, 91  
 Jiang, L., Egami, E., Fan, X., et al. 2013, *ApJ*, **773**, 153  
 Jiang, T., Malhotra, S., Yang, H., et al. 2019, *ApJ*, **872**, 146  
 Kennicutt, R. C. 1998, *ApJ*, **498**, 541  
 Kim, K., Malhotra, S., Rhoads, J. E., et al. 2018, *ApJ*, **867**, 118  
 Kolaczyk, E. D. 1997, *ApJ*, **483**, 340  
 Lee, J. C., Gil de Paz, A., Tremonti, C., et al. 2009, *ApJ*, **706**, 599  
 Lintott, C. J., Schawinski, K., Slosar, A., et al. 2008, *MNRAS*, **389**, 1179  
 Malhotra, S., Rhoads, J. E., Finkelstein, S. L., et al. 2012, *ApJL*, **750**, L36  
 Marchi, F., Pentericci, L., Guaita, L., et al. 2019, *A&A*, **631**, A19  
 Meurer, G. R., Heckman, T. M., Lehnert, M. D., Leitherer, C., & Lowenthal, J. 1997, *AJ*, **114**, 54  
 Neufeld, D. A. 1991, *ApJL*, **370**, L85  
 Orlitová, I., Verhamme, A., Henry, A., et al. 2018, *A&A*, **616**, A60  
 Paulino-Afonso, A., Sobral, D., Ribeiro, B., et al. 2018, *MNRAS*, **476**, 5479  
 Petrosian, V. 1976, *ApJL*, **209**, L1  
 Pirzkal, N., Malhotra, S., Rhoads, J. E., et al. 2007, *ApJ*, **667**, 49  
 Rhoads, J. E., Malhotra, S., Dey, A., et al. 2000, *ApJL*, **545**, L85  
 Ritondale, E., Auger, M. W., Vegetti, S., et al. 2019, *MNRAS*, **482**, 4744  
 Salpeter, E. E. 1955, *ApJ*, **121**, 161  
 Shibuya, T., Ouchi, M., Harikane, Y., et al. 2019, *ApJ*, **871**, 164  
 Shibuya, T., Ouchi, M., Nakajima, K., et al. 2014, *ApJ*, **788**, 74  
 Shimasaku, K., Fukugita, M., Doi, M., et al. 2001, *AJ*, **122**, 1238  
 Silich, S., & Tenorio-Tagle, G. 2018, *MNRAS*, **478**, 5112  
 Song, M., Finkelstein, S. L., Gebhardt, K., et al. 2014, *ApJ*, **791**, 3  
 Tremonti, C. A., Heckman, T. M., Kauffmann, G., et al. 2004, *ApJ*, **613**, 898  
 Verhamme, A., Orlitová, I., Schaerer, D., et al. 2015, *A&A*, **578**, A7  
 Verhamme, A., Orlitová, I., Schaerer, D., et al. 2017, *A&A*, **597**, A13  
 Verhamme, A., Schaerer, D., & Maselli, A. 2006, *A&A*, **460**, 397  
 Whitaker, K. E., van Dokkum, P. G., Brammer, G., et al. 2012, *ApJL*, **754**, L29  
 Wood, K., & Loeb, A. 2000, *ApJ*, **545**, 86  
 Yang, H., Malhotra, S., Gronke, M., et al. 2016, *ApJ*, **820**, 130  
 Yang, H., Malhotra, S., Gronke, M., et al. 2017, *ApJ*, **844**, 171